AERODYNAMIC EFFECTS OF TRANSITION STRIP APPLICATION ON A MULDICON WING IN LOW-SPEED WIND TUNNEL TESTING

Bilal Haider, Shuhaimi Mansor, Shabudin Mat*, Wan Zaidi Wan Omar, Nazri Nasir

UTM Aerolab, Universiti Teknologi Malaysia, 81310 UTM Johor Bahru, Johor, Malaysia

Article history
Received
8th May 2026
Received in revised form
26th May 2026
Accepted
27th May 2026
Published
15th June 2026

*Corresponding author
shabudin@utm.my

ABSTRACT

Low-sweep, blunt-leading-edge unmanned combat aerial vehicle (UCAV) configurations exhibit complex vortex separation and inconsistent aerodynamic behaviour at moderate-to-high pitch angles. This study experimentally investigates the effects of leading-edge transition strips on a lambda-planform MULDICON AVT251 wing with a 53° blunt leading-edge sweep. Wind-tunnel tests were conducted in the UTM Low-Speed Wind Tunnel at Reynolds numbers of $3.00 \times 10^5$to $4.50 \times 10^5$and pitch angles from $-4°$to $30°$. Lift, drag, pitching-moment coefficients, and surface flow visualisation were analysed for free-transition, 2D-transition, and 3D-transition cases. The results show that transition-strip type strongly affects the onset and progression of leading-edge vortex separation. The 3D transition strip produced a smoother and more consistent aerodynamic response than the free- and 2D-transition cases, particularly in the pitching-moment coefficient. For the 3D transition case, stall occurred at $\alpha = 24°$, with $C_L = 1.0183$, while $C_m$remained more predictable up to $\alpha = 22°$. The findings indicate that the pitching-moment coefficient is highly sensitive to flow topology and vortex-separation behaviour. Overall, the 3D transition strip is recommended to establish a repeatable baseline for future MULDICON flow-field measurements and CFD validation at subsonic.

KEYWORDS

MULDICON wing; Rounded leading-edge; Vortices; Flow separation; Pitching moment coefficient; Wind Tunnel (W/T) Experiments; Transition strips.

INTRODUCTION

The study of low-aspect-ratio delta wing configurations, which are dominated by vortex flow separation, has been of prime interest in aerodynamic research for decades due to the additional nonlinear vortex lift generated by the flow [1, 2]. A major advantage of vortex lift is that it remains effective at high pitch angles, where conventional aircraft would normally stall. The high-pitch-angle flight is frequently encountered during the landing and take-off phases of a flight and during combat manoeuvring [3]. The flow topology over high-sweep delta wings, characterised by sharp leading-edge vortex formation, has been extensively investigated and is well understood, with flow separation geometrically fixed [4, 5], whereas flow over low-sweep delta wings is complex and nonlinear [6]. The recent interest in UCAVs has resulted in a need to further understand the topology of the flow over low sweep delta wings with blunt leading edges [7, 8]. Current UCAV configurations often use LE sweep angles between 45º and 60º [9].

Low-sweep wing configurations exhibit different vortex onset and progression than high-sweep wings with sharp leading edges. The leading-edge vortex is not fixed at the apex but a located downstream and moves towards the apex as the pitch angle increases. The flow structures

occur much closer to the wing surface, and the vortex strength is also reduced [6, 10, 11]. Complex vortexes with dual structures are formed for the low sweep wing with the leading-edge vortex moving inboard and away from the wing surface with increases in pitch angle, and the vortex breakdown starts earlier, and the shear layer separation line is not rectilinear [12-14].

For blunt-leading-edge (BLE) configurations, Reynolds-number effects become more noticeable because the boundary-layer state influences the onset and progression of vortical flow separation [15]. The leading-edge radius of the wing configuration also has a significant impact on vortical flow separation [16]. For the wind tunnel (W/T) experimental study of low-sweep wing configurations, a fixed boundary-layer transition location from laminar to turbulent flow is preferred. Specifically for the wing configurations that are analysed in low-speed W/T, the application of transition strips near the leading edge (LE) of the wing is of prime importance as the possible laminar flow region can be avoided and the experimental results can be used for validation purposes in the CFD analysis using the fully turbulent Reynolds Averaged Navier Stokes (RANS) equations [8, 17]. For BLE vortex-dominated wings, leading-edge transition strips can influence both the boundary-layer state and the onset of vortex-induced flow separation. Therefore, the flow-separation dependence on the LE transition strips for blunt leading-edge low-sweep delta-wing configurations is considered in the present article.

At low pitch angles, the flow over the low sweep delta wing is attached, which results in consistent and predictable aerodynamic stability derivatives, whereas at moderate and higher pitch angles, the flow doesn't remain attached, and the onset and progression of the vortex separation occur, which results in highly complex and nonlinear flow. The unsteadiness and uncertainties of the flow topology at high pitch angles, such as leading-edge vortex separation, vortex breakdown, and shear-layer reattachment, result in highly nonlinear, fluctuating, and discontinuous aerodynamic stability derivatives. The unsteadiness and uncertainties of the flow for low-sweep delta wings at higher pitch angles need to be mitigated by either controlling the vortical flow or delaying the onset and progression of vortex flow separation to higher pitch angles, thereby making aerodynamic stability derivatives more consistent and predictable [18, 19]. Stability and Control CONfiguration (SACCON), Applied Vehicle Technology (AVT-161), is a UCAV configuration with a low-sweep, lambda-planform, with a leading-edge (LE) and trailing-edge (TE) sweep angles of 53° [17, 20]. Flow fields for SACCON are vortex-dominated and complex, with multiple vortices forming over the surface, which makes the stability derivative C_(m_α) highly fluctuating and discontinuous at moderate to a higher angles of attack, and it shows a typical dip for 14° ≤α≤ 19° in the curve. The dip results due to the flow topology on the wing's upper surface. Therefore, the mentioned range of the pitching moment is very sensitive to the flow parameters, which in turn depend upon the geometric shape of the configuration[17, 21]. AVT183 Diamond wing is a blunt leading edge configuration with relatively simple flow topology compared to the complex flow topology of the SACCON AVT-161, and emphasised one typical flow phenomenon of SACCON, i.e. flow separation onset and progression for blunt leading edge contour[22]. The flow field around the blunt LE AVT183 wing investigated experimentally and computationally confirms that the onset of vortex formation is delayed to higher pitch angles [23, 24].

The major development for the Diamond wing was that, by increasing the wing's span and applying blunt leading edges, the leading-edge vortex flow separation is delayed to higher AOA, with a more consistent and predictable derivative. So the basic SACCON platform needed to be modified to mitigate uncertainties in the flow, making the derivative C_{m_α}more consistently and predictably at high AOA. Therefore, SACCON was modified to the MULDICON AVT251 platform to delay the onset and progression of flow separation at a higher pitch angle, thereby making it possible, by increasing the wing's span and applying blunt leading edges, to delay the leading-edge vortex flow separation to a higher AOA, with a more consistent and predictable derivative. C_{m_α} more consistent and predictable at a higher pitch angle [19, 25]. The MULDICON configuration includes 53º LE and 30º TE sweeps, as shown in Figure 2. Initial CFD results show consistent and predictable C_(m_α) derivative at higher pitch angle, α, for the MULDICON wing [25-28]. The aerodynamic coefficients and flow topologies over the MULDICON AVT251 wing need to be experimentally studied in detail to validate the extended linear aerodynamic stability.

Preceding computational fluid dynamics (CFD) studies of the MULDICON AVT251 flow field's characteristics are reported in [25-28]. Experimental studies are necessary to validate the computational results for the MULDICON AVT251. During the experimental investigations, the boundary layer in the wind tunnel must be tripped. 3D transition strips showed a successful transition from laminar to turbulent with the disturbance

height of 0.5mm located at both the upper and lower side at a 2mm arc distance from the leading edge. The flow around the MULDICON AVT251 wing configuration with 3D transition strips, a height of 0.5mm at Re = 3.75E+05, was defined as the validation case for fully turbulent CFD simulations. Besides that, the W/T studies offer a detailed experimental database for CFD validation, applicable to separation onset and progression, as well as to leading-edge vortex formation, over smooth, moderately swept surfaces and a low-aspect-ratio wing with a blunt LE shape.

This study considers key W/T experimental results to predict the influence of transition strips near the Leading Edge in low-sweep-lambda UCAV configurations. This research covers the static portion of the UTM-LST testing. Flow visualisation of the free transition MULDICON wing configuration is carried out to highlight the complex vortex flow onset and propagation as the pitch angle, α, increases. The study of the effects of different transition strips on the aerodynamic coefficients is presented in detail, and the repeatability of the W/T measurements is verified. The influence of Reynolds number variation is studied in detail for the free-transition and 3D-transition wing configurations. Finally, the flow topology is correlated with the pitching moment coefficient to highlight the pitching moment's sensitivity to vortex onset and propagation.

Experimental Test Set-Up

This section presents the experimental test setup, the MULDICON model design, and the transition strip methods used. Following that, the study describes the wind tunnel measurements and the data analysed. Finally, the results were presented and discussed to provide recommendations for a subsequent, thorough study of the flow topology using a Particle Image Velocimetry (PIV) or hot-wire anemometry, along with dynamic measurements.

The studies are conducted at the Universiti Teknologi Malaysia Low-Speed Wind Tunnel (UTM-LST) facility, located at Aerolab, the School of Mechanical Engineering, Universiti Teknologi Malaysia. The current experimental setup, the MULDICON wing design, the transition strip applications, and the measurement techniques are defined subsequently.

Wind Tunnel (W/T) Testing was performed in the Universiti Teknologi Malaysia Low-Speed wind Tunnel (UTM-LST) (a closed circuit subsonic wind tunnel) as shown in Figure 1. The rectangular test section of UTM-LST has a test volume of 16.5 m^3 (1.5 m height x 2.0 m wide x 5.5 m length) with a maximum wind speed of 80 m/s [29]. Flow quality is excellent, having flow uniformity variation < 0.15%, turbulence < 0.06%, flow angularity uniformity variation < 0.15% and temperature uniformity variation < 0.2°C [30]. The flow has to pass through three screens before entering the test section, then through a honeycomb. Together, they act as straighteners and turbulence filters, reducing turbulence and flow angularity. The maximum speed of the wind tunnel is 82 m/s.

MULDICON Wind tunnel model

The 3-dimensional Wind Tunnel MULDICON model is fabricated as a full-span model, using Polylactide Polylactic acid (PLA+) material. Figure 2 and Table 1 summarise the MULDICON W/T model platform. The MULDICON configuration includes a 53º LE sweep and a 30º TE sweep. Overall, the MULDICON wing features centre-line profile A-A, profile B-B and profile C-C of chord lengths 0.391, 0.234 and 0.135 m, respectively, as shown in Figure 2. The W/T model span b = 0.6 m.

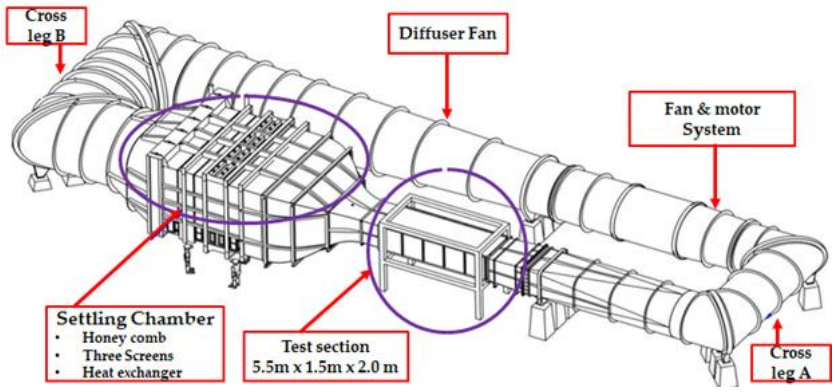

Figure 1: UTM-LST wind tunnel facility.

Table 1: MULDICON W/T model planform parameters.

$\emptyset_{le}$	$\emptyset_{te}$	c_r (m)	c_{mac} (m)	c (m)	b (m)	X_{mrp} (m)	S_{ref} (m^2)
53°	30°	0.391	0.234	0.135	0.600	0.234	0.1216

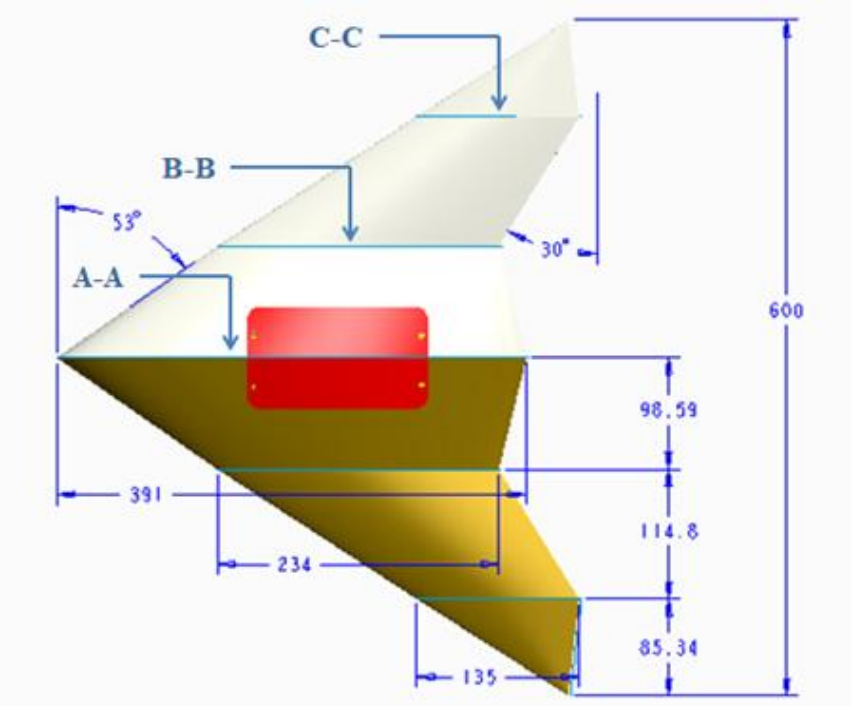

Figure 2: Geometric details of MULDICON W/T model.

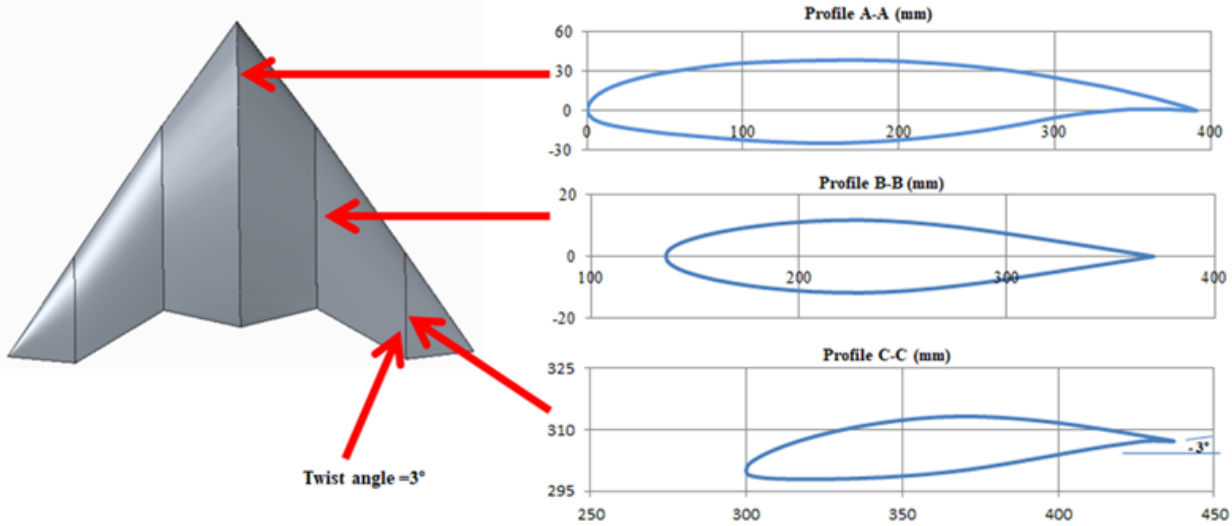

Figure 3: MULDICON Wing Section profile for wind tunnel model.

Figure 3 shows the MULDICON model profile cross-section, where aerofoil A-A is a supercritical Dornier, B-B is an asymmetric NACA 64A010, and C-C is a slightly cambered aerofoil NACA 65A410 with an LE radius to chord ratio of rle/c = 0.51%. This ratio is constant along the wingspan for the

centre section (A-A) and wing-body interphase (B-B) and then decreases linearly from section C-C to become sharp at the wingtip [19]. The three-degree twist angle is also applied from Section C-C.

Pitch angle variation mechanism

Figure 4 shows the mechanism for varying the pitch angle α, designed for the MULDICON W/T model for testing at UTM-LST. Pitch angle is varied by the pitch angle variation device, which is capable of varying the pitch angle α from -25 to +35 degrees. The pitch angle is measured using an inclinometer referenced to a flat plate in the model body, as shown in Figures 2 and 3. The desired pitch angle, α, is ensured by tightening the pitch angle variation device with the strut and is further assisted by a locking pin, a nut and a bolt.

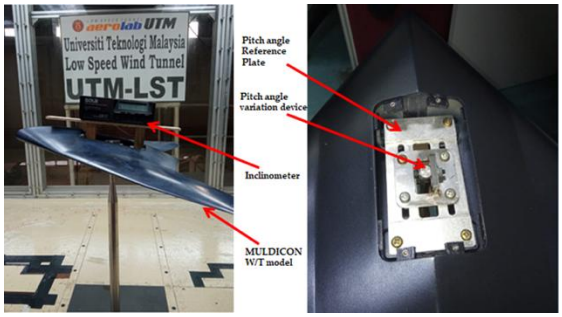

Figure 4: Pitch angle, α, variation mechanism design.

Transition strips

To fix the location of the transition from laminar to turbulent boundary layer, an artificial roughness termed transition strips is added to the models. This process energises the boundary layer and prevents flow separation [31]. Many types of transition strips can be used, including boundary-layer trips (wires, tape, strips, grit, tube, or rod), as discussed in detail in the literature [32-34]. In the current experimental investigations, two different types of transition strips were investigated. One of the transition strips, the 2D transition strip, was applied. The 2D transition strips consist of two-dimensional rectangular printed circuit drafting tape or chart tape. The 2D transition strips consist of multiple layers of tape. The other transition strips, known as 3D transition strips, were applied. The 3D transition strips are rectangular strips with an adhesive layer and carborundum particles. Barlow and Rae Jr. [32] discuss the advantages and disadvantages of both methods, including application, coating, and measurement repeatability issues. Recently, both types of transition strips have been widely used in experimental studies aimed at generating high-quality data to validate numerical results. The 2D transition tapes have been extensively used previously for research purposes [35]. The carborundum grit, 3D transition strips were used as the flow tripping devices in the low-speed wind tunnel testing for the low sweep lambda wing configurations SACCON AVT161and Diamond AVT183 wings configurations[36, 37].

Estimation of Critical Roughness Height for Transition Strips

To select the initial design of the transition strips, including the position, height, and extent of the strips for application to the MULDICON wing configuration, some basic boundary-layer flow equations for a flat plate without a pressure gradient and at 0º incidence were calculated for comparison [31, 38]. The critical transition strip is the minimum transition strip height required to cause the transition from laminar to turbulent boundary-layer flow. For the smaller transition strip heights, the skin friction coefficient (C_f) is not affected, as the laminar boundary layer becomes insensitive to the transition strip's effects. Eq. (1) is used to calculate the skin friction coefficient for the laminar boundary layer flow.

$$C_f = \frac{1.328}{\sqrt{Re}} \tag{1}$$

The transition from the laminar to turbulent boundary layer flow is initiated for larger transition strips heights than the boundary layer height. Eq. (2) gives the critical roughness height which is needed for the transition from laminar to the turbulent flow. Hence the critical transition strip (k_{crit}) is dependent on the boundary layer run length (x) and the actual flow state involving the wind speed (U) and the kinematic viscosity (v). For the present investigation, the transition strips location required close to the leading edge (LE) of the MULDICON wing surface, k_{crit} ≈ 190 μm is estimated.

$$k_{crit} = 26.x^{\frac{1}{4}}(\frac{v}{U})^{\frac{3}{4}} \tag{2}$$

An additional evaluation of a fully developed turbulent boundary layer can be made. If the viscous sublayer of the boundary layer is not exceeded by the transition strip heights, the surface is hydraulically smooth and represented by Eq. (3), where the skin friction is a function of the

Reynolds number. Otherwise, it is referred to as the hydraulically rough, as shown by Eq. (4), and is independent of the Reynolds number and depends only on the relative wall roughness (k/l). The differentiation is based on the permissible roughness height (k_{per}) , as reported in Eq. (5) [39].

$$C_f = \frac{0.455}{(lg.Re)^{2.58}} \quad (3)$$

$$C_f = 0.024.\left[\frac{k}{l}\right]^{\frac{1}{6}} \quad (4)$$

$$k_{per} = \frac{100.v}{U} \quad (5)$$

The freestream conditions in Table 3 for the MULDICON W/T model yield a value of k_{per} ≈ 85 μm. As the flow transition devices are applied very close to the leading edge of the MULDICON wing, the area is strongly affected by the negative pressure gradient induced by flow acceleration. Since the flat-plate estimate provides only an initial approximation and does not fully represent the three-dimensional blunt-leading-edge MULDICON geometry, a conservative transition-strip height of 500 µm was selected. This value is higher than the estimated critical roughness height to ensure robust boundary-layer tripping near the leading edge under local acceleration and pressure-gradient effects. The selected height is also consistent with previous low-speed wind-tunnel studies using carborundum grit transition strips on comparable low-sweep configurations.

Applied Transition strips

Figure 5 summarises the subsequent transition-strip cases applied to the MULDICON W/T model. In general, the calculation presented here provided only initial estimates of the transition strips and cannot be directly applied to the MULDICON wing with a blunt leading-edge contour. For 2D transition strips, different adhesive layers of masking tape are applied to achieve the required transition height, as shown in Figure 5 (a). Similarly, for the 3D transition case, an adhesive layer and a roughness height with carborundum grit were applied, as shown in Figure 5 (b). The geometrical properties of each test case are documented in Figure 6 and Table 2. On the left side of Figure 6 (a), an overall overview of the 2D transition strip application at the leading edge is shown. The 2D transition strip was applied to both the upper and lower wing surfaces. The 2D transition strip was attached around the leading edge of the MULDICON wing up to l_{arc}/c_{mac}=1.1% along the arc length on both the upper and lower sides of the MULDICON wing. Similarly, the 3D transition strip, better known as carborundum grit, was attached around the leading edge of the MULDICON wing up to l_{arc}/c_{mac}=0.86% along the arc length on both the upper and lower sides of the MULDICON wing. Figure 6 (b), further highlights the structure of the adhesive layer and the carborundum grit of the 3D transition strip.

In Figure 6, the streamline flow around the leading edge at pitch angle α is shown for both types of transition strips. To study the onset of flow separation on the MULDICON wing, a turbulent boundary layer is desired over the leading edge. For this reason, the flow was initially tripped at the lower surface of the MULDICON wing as shown on the right side of Figure 6. The dividing streamlines on the pressure side of the airfoil, where the flow splits into suction- and pressure-side flows, generally move farther downstream as the pitch angle, α, increases.

Aerodynamic force measurement

To acquire the aerodynamic force and moment coefficients for the MULDICON W/T model, an external six-component balance was used to measure the forces and moments. The external balance provides the forces and moments in the x, y, and z axes, respectively. The MULDICON W/T model is mounted on a vertical strut connected to a JR3 6-component balance, placed under the wind tunnel floor, as shown in Figure 7 [40, 41].

The forces (Lift, Drag, Side force) have the same axis for the balance and the W/T model. Where lift (L) is the force in the y-direction perpendicular to the wind flow direction, and drag (D) is the force in the x-direction parallel to the wind flow direction, as shown in Figures 2 to 7. The Lift and drag forces can be converted to the lift coefficient and drag coefficient by Eq. (6) and Eq. (7), where ρ is the air density ($^{Kg}/_{m^3}$), S is wing surface area (m^2).

Table 2: Geometrical properties of the applied trip strips at the MULDICON W/T model.

Transition strip case	2D (adhesive) (μm)	Carborundum grit (μm)	Total height (μm)
Free transition	0	0	0
2D transition	500	0	500
3D transition	150	350	500

(a) (b)

Figure 5: Summary of the transition strips applied to the MULDICON wing: (a) 2D adhesive transition strip at the leading edge and (b) 3D carborundum-grit transition strip at the leading edge.

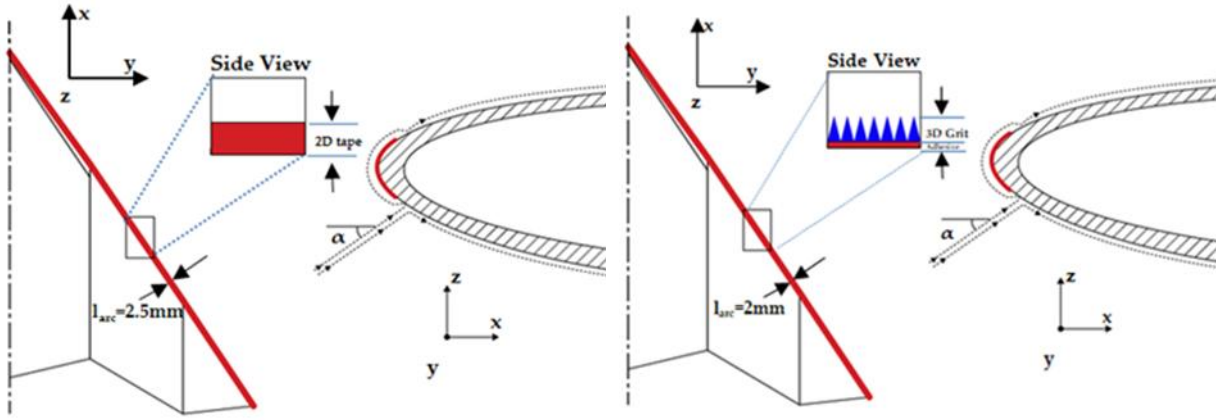

(a) (b)

Figure 6: Geometric properties of the applied transition strips on the MULDICON wing: (a) 2D transition strips applied on the upper and lower wing surface (b) 3D transition strips applied on the upper and lower wing surface.

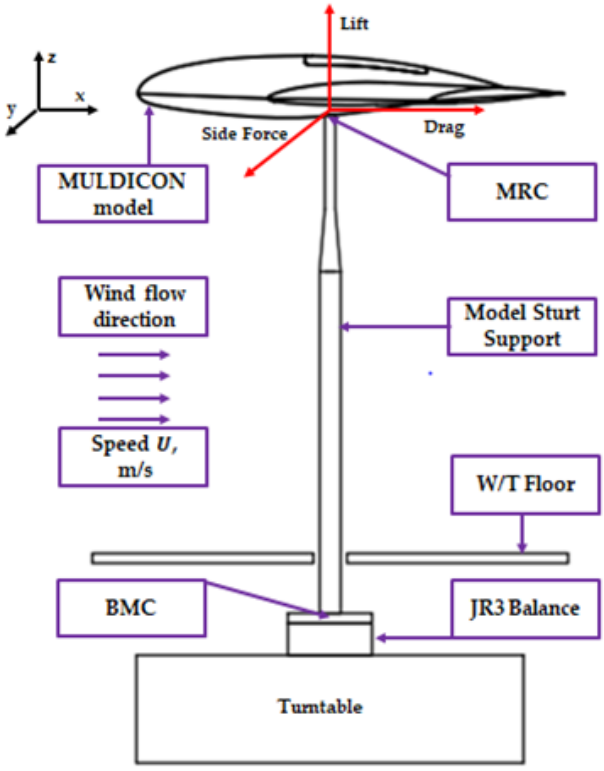

Figure 7: Flow diagram of Model in the test section.

The forces, namely lift, drag, and side force, are aligned with the balance and wind-tunnel model axes, where lift (L) is the force in the y-direction perpendicular to the wind flow direction, and drag (D) is the force in the x-direction parallel to the wind flow direction, as shown in Figure 7. In Figure 7, MRC refers to the moment reference centre used for calculating the pitching moment coefficient, while BMC refers to the balance moment centre of the external six-component balance. The Lift and drag forces can be converted to the lift coefficient and drag coefficient by Eq. (6) and Eq. (7), where ρ is the air density (kg/m^3), S is the wing surface area (m^2).

$$C_L = \frac{L}{1/2\,\rho S U^2} \tag{6}$$

$$C_D = \frac{D}{1/2\,\rho S U^2} \tag{7}$$

$$C_m = \frac{PM_{BMC}}{1/2\,\rho S c U^2} \tag{8}$$

Similarly PM_{BMC} , the pitching moment of the W/T model can be converted to the pitching moment coefficient C_m by Eq. (8), where c is the mean aerodynamic chord length (m). Therefore, for the W/T model, the moment centre can be calculated by substituting Eq. (9) into Eq. (8), and the final equation for the pitching moment coefficient is given in Eq. (10) below.

$$PM_{MRC} = PM_{BMC} - z_{MRC} D \tag{9}$$

$$C_{my} = \frac{PM_{MRC}}{1/2\,\rho S c U^2} \tag{10}$$

where $z_{MRC}$is the vertical distance between the balance moment centre and the model moment reference centre.

As extensive wind tunnel testing is involved so it is necessary to consider the blockage correction. The wind tunnel total wake and solid blockage correction are given by Eq. (11) shown below [32].

$$\varepsilon_t = \frac{1}{4}\frac{Model\ Frontal\ Area}{Test\ section\ Area} \tag{11}$$

The maximum possible unnecessary correction limit was 7.5%. By applying Eq. (11) to the W/T MULDICON model we get:

$$\varepsilon_t = \frac{1}{4}\left[\frac{0.1216}{3.0}\right]$$
$$\varepsilon_t = 0.0101 = 1.01\%$$

Table 3: Testing Reynolds Number.

Speed (U), m/s	Reynolds number (Re)
20	3.00E+05
25	3.75E+05
30	4.50E+05

Thus, we can say that the correction for the blockage is negligible. Whereas the strut interference was measured by mounting the strut without the W/T model, and all readings for the model are corrected for the Strut interference. Aerodynamic loads from the JR3 balance will be logged by LabVIEW. The wind tunnel testing is conducted over the Reynolds number range given in Table 3. Four different sets of data points were logged, with each data point time-averaged over 12 seconds, yielding a set of data measurements. The wind tunnel testing also showed good repeatability. It is noted that repeatability was assessed using the standard deviation and relative standard deviation (RSD) of repeated time-averaged force and moment measurements.

In this study, the Reynolds numbers of 3.00×10^5, 3.75×10^5, and 4.50×10^5were selected to represent the achievable operating range of the UTM-LST facility for the present model scale while maintaining acceptable blockage and balance measurement sensitivity. The intermediate case, $Re = 3.75 \times 10^5$, was used as the primary comparison condition for evaluating the effects of transition-strip type.

Surface Oil Flow Visualisation

Petroleum lubricating oil 10W-30 made white by mixing titanium dioxide (TiO2) (mixing ratio of 13 grams of TiO2 to 30 millilitres of lubricating oil) was used for surface flow visualisation [32]. The white mixture was applied in a dot-matrix pattern on the W/T model surface. The mixture would move or flow across the W/T model surface as wind speeds increase over the wing model; hence, the surface flow topology and pattern can be visualised.

Wind tunnel condition and errors

The experiment on the AVT251 MULDICON wing was conducted in UTM-LST at 20, 25, and 30 m/s, corresponding to Reynolds Numbers (Re) of 3.00E+05, 3.75E+05, and 4.50E+05, based on the mean aerodynamic chord c_{mac} = 0.234 m. During the experiments, the pitch angle, α, was varied between -4° and 30°. The wind tunnel blockage is 1.01%, which is very small, such that blockage correction is not required for this experiment. The wall interference correction is also small and negligible. The strut interference was measured without the W/T model, allowing the aerodynamic forces and moments readings for the W/T model to be corrected. The wind tunnel testing also showed good repeatability.

RESULTS

Surface flow visualization results, the effects of the transition strips, the effect of the Reynolds number and their uncertainty analysis with the error bars are presented in this section while running the UTM-LST, for the pitch angle α = -4° to 30° with each increment of 2 degrees at Reynolds number Re of 3.00E+05, 3.75E+05 and 4.50E+05 for speed U of 20, 25 and 30 m/s respectively.

Surface oil Flow Visualisation

Figure 8 shows the surface oil flow visualisation for the free transition MULDICON AVT251 wing at 4.50E+05, for α=5°,10°,15° and 20° with the yaw angle, β = 0°. For α=5° with the yaw angle, β=0°. In this study, the inner vortex refers to a vortical structure that forms closer to the centreline or the inboard region of the wing. The outer or tip vortex refers to the vortex structure developing near the outer wing or tip region. The leading-edge vortex is the separated shear-layer vortex generated along the leading edge that progresses upstream and inboard as the pitch angle increases. Figure 8 (a) shows that an inner vortex had developed, as previously also shown by Ol and Gharib [11] and Taylor and Gursul [42] for the low sweep delta wings, and it can be seen very clearly that the outer vortex at the wingtip is not yet present at α=5°. Hence, it is very clear from Figure 8 (a) that the inner vortex develops earlier than the leading-edge vortex for a low sweep configuration.

Similarly, we can also visualise a small weak apex vortex at a certain location aft of the apex as also indicated previously computationally by Nangia, Ghoreyshi [27] the MULDICON wing.

Figure 8 (b) for α=10° with the yaw angle, β=0°, shows the flow separation near the wingtip, which confirms the onset and progression of the leading edge vortex separations previously shown by Gordnier and Visbal [13] and Loechert, Huber [43]. Whereas the inner vortex, which was visible at α=5°, now appears to vanish at α=10° as previously confirmed by Ol and Gharib [11] and Visbal [5].

The apex vortex, observed at α=5°, has moved forward towards the wing's apex at α=10°. Along the wing trailing edge, the outflow from the wing surface has established into the trailing edge separation at α=10°, where the trailing edge flow is swept spanwise towards the wingtip at the upper surface of the model. Figure 8(c) for α=15° with the yaw angle β=0° shows that the leading-edge vortex has moved upstream and inboard, and behind the leading-edge vortex, there exists a low-shear region. The apex vortex has moved further towards the wing's apex at α=15°.

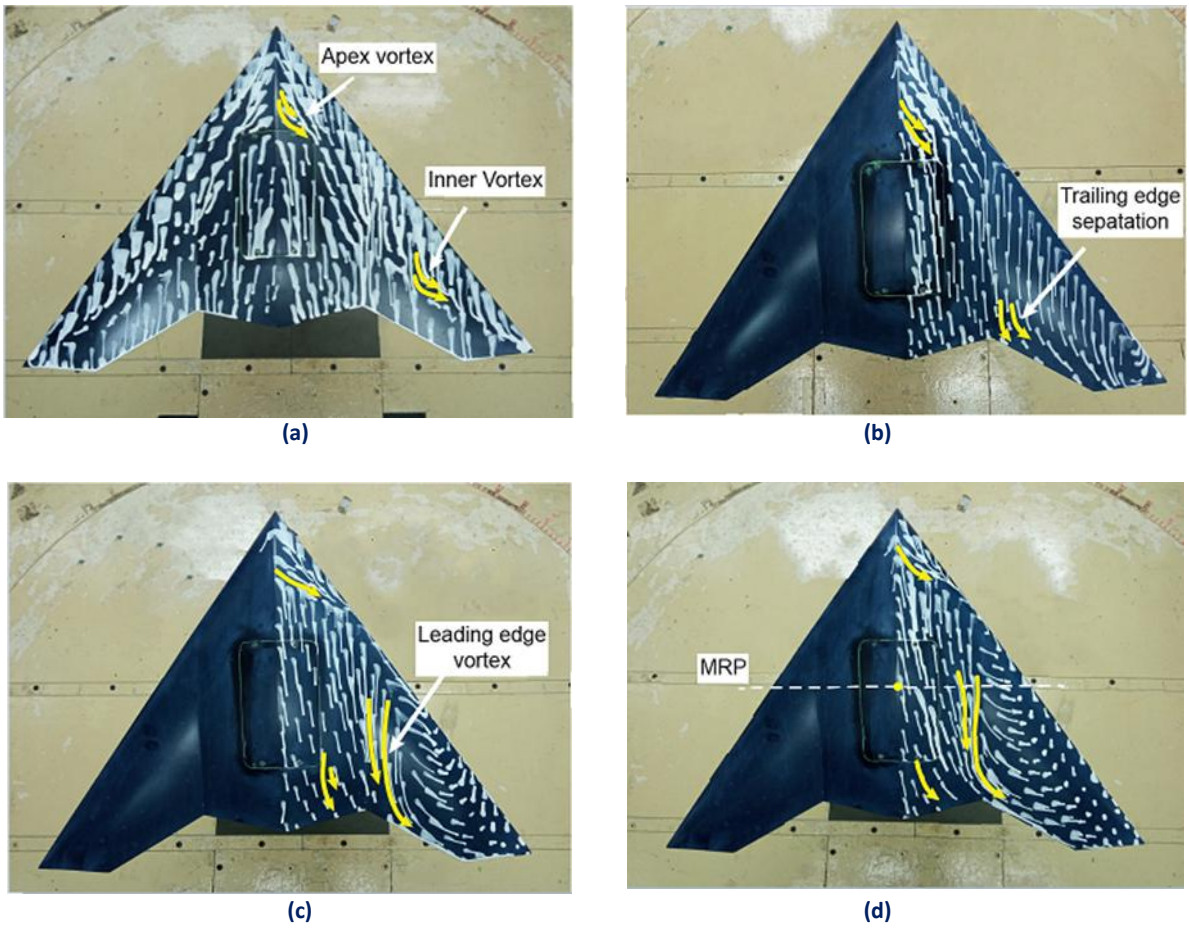

Figure 8: Surface oil flow visualization at Re = 4.50E+05 for (a) α=5°, (b) α=10°, (c) α=15° and (d) α=20°

The trailing-edge flow separation has extended inboard towards the wing centreline at α=15°. Figure 8 (d) for α=20° with the yaw angle, β=0°, shows the leading-edge vortex advances further towards the apex and passes the moment reference point (MRP)of the wing, and towards the inboard sections of the wing, at α=20° and the primary separation line of the shear layer is not rectilinear, as also previously confirmed Renac, Barberis [12]. The low shear region behind the leading edge vortex has also increased. The apex vortex has further moved towards the wing apex, and the apex vortex structure appears to be very small at α=20°. The trailing-edge flow separation has also extended further inboard towards the wing centreline at α=20°.

The effects of different transition strips on the lift drag and the pitching moment and their uncertainty are discussed and analysed with the help of standard deviation data by plotting the error bars in this section while running the UTM-LST, for the pitch angle α = -4° to 30° with each increment of 2 degrees at Reynolds number, Re of 3.75E+05 for speed U of 25 m/s.

Aerodynamic Coefficients

The influence of different types of transition strips at Re of 3.75E+05 corresponding to the speed of 25 m/s on the lift coefficient C_L is presented in Figure 9, which shows that there is no effect of the transition strips on the lift coefficient C_L for α = -4 to 8º. Both the 2D and the 3D applied transition strip result in a similar C_L curve and do not show noteworthy differences to the free transition case for pitch angle, α = -4 to 8º. Figure 9 shows that for α = 8 to 16º, the lift curve is similar for the free transition and the 2D transition case, whereas for the 3D transition case a little higher lift is generated for α = 8 to 16º compared to the free transition and the 2D transition case. For α = 16 to 30º, Figure 9 shows that the lift curve for the free transition case is not consistent and highly fluctuating and it is not possible to locate the stall angle for the free transition case, even for the 2D transition case for α = 16 to 30º, the lift curve is not consistent and there are still some fluctuations in the curve which make it difficult to predict the actual stall angle of the MULDICON wing. Whereas Figure 9 shows that for α = 16 to 30º, the 3D transition case gives a rather smooth and consistent lift curve and the stall for the MULDICON wing occurs at α = 24º where the C_L = 1.0183. Hence for the 3D transition case, the lift curve is smooth and consistent with a slightly higher lift generated for the region of α = 8 to 16º and the stall occurs at α = 24º.

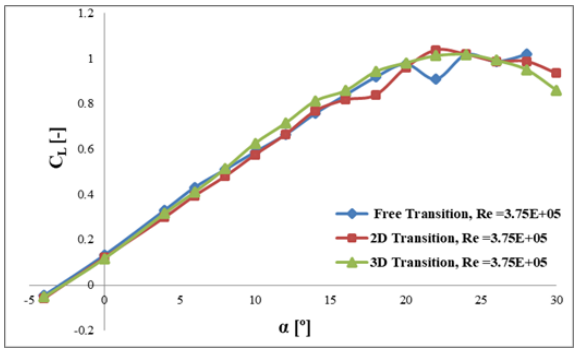

Figure 9: Lift Coefficient, C_L vs pitch angle α.

The influence of different types of transition strips at Re of 3.75E+05 corresponding to the speed of 25 m/s on the drag coefficient C_D is presented in Figure 10. The drag coefficient C_D is affected by using different transition strips as shown in Figure 10 (a), and the slight deviations for the C_D are observed for the complete range of the pitch angle,α and the maximum deviations among the transition strips cases are for the higher pitch angle i.e. α >20º where the lowest C_D is for the 3D transition strips. Figure 10 (b) shows the detailed view of the differences occurring among the various transition strips with the low pitch angle, α more precisely. The effect of the different transition strips is more obvious in Figure 10 (b), where the zero drag coefficient $C_{D,0}$ is the lowest for the free transition case and the drag coefficient for the cases with the forced transition is higher than that for the free transition.

This overall highlights the influence of the use of the transition strips and specifies the presence of; at least, partially laminar flow regions on the MULDICON wing surface without the use of the transition strips. The skin friction for the complete laminar flow according to the Eq. (1) is $C_f \approx 0.0022$ which is very small compared to the value from graph Figure 10 (b), which confirms that this partially laminar region can't be very widespread and should be limited to small regions. In general, the experimental analysis confirms an increase of the zero-drag coefficient $C_{D,0}$ with increasing transition strip height.

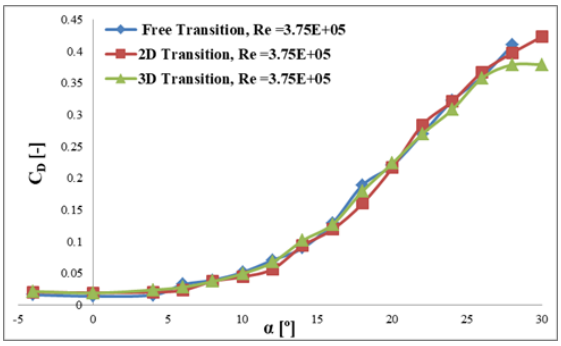

(a)

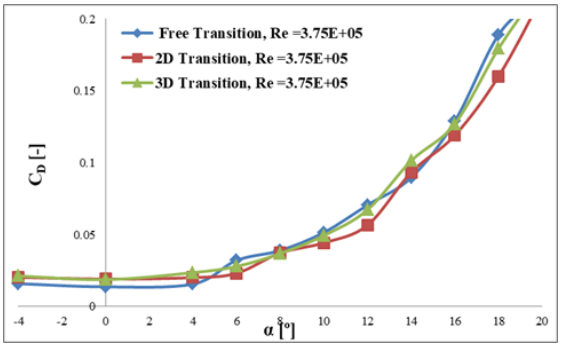

(b)

Figure 10: Drag coefficient,C_D VS pitch angle, α.

The influence of different types of transition strips at Re of 3.75E+05 corresponding to the speed of 25 m/s on the pitching moment coefficient C_m is plotted in Figure 11 (a) for the reference point at the mean aerodynamic chord, Figure 11 (a) shows

that there is a deviation in the pitching moment coefficient C_m for the different transition strips from each other with increasing pitch angle,α and all cases C_m curves increase monotonically up to α ≈ 22º, there is a significant deviation for different transition cases when compared to the free transition case. For pitch angle higher than α > 5º, all the C_m curves become nonlinear as shown very clearly in Figure 11 (a). The deviations of the C_m curves from each other are primarily due to the different vortex flow separation onset and progression near the MULDICON wing leading edge as discussed in detail in the Discussion section.

For higher pitch angle, α >17º, Figure 11 (a) indicates that the free transition and the 2D transition C_m curves are no more increasing monotonically and there is a steep pitch up pitching moment possible due to the upstream movement of the leading edge vortex and the vortex breakdown which indicates a highly inconsistent and nonlinear pitching moment for the free transition and the 2D transition cases at higher pitch angle. But for the 3D transition case, the pitching moment curve continues to increase smoothly and consistently up to a pitch angle of α = 24º, indicating a consistent and predictable pitching moment coefficient for the 3D transition wing. Figure 11 (b) confirms that the pitching moment coefficient C_m becomes non-linear with the pitch angle, α, for all the transition cases. Figure 11 (b) shows that normally the derivative $C_{m,\alpha}$ increases with the pitch angle,α increase for all the transition cases. For free transition case the trend of the increase in $C_{m,\alpha}$ with the pitch angle, α is interrupted between α=4-6º, α=8-10º and α=12-14º for which a slight decrease in $C_{m,\alpha}$ is noticed.

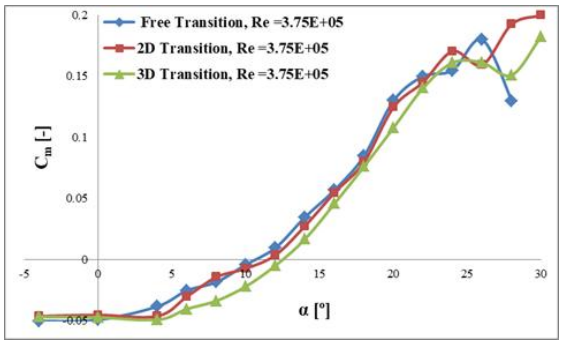

(a)

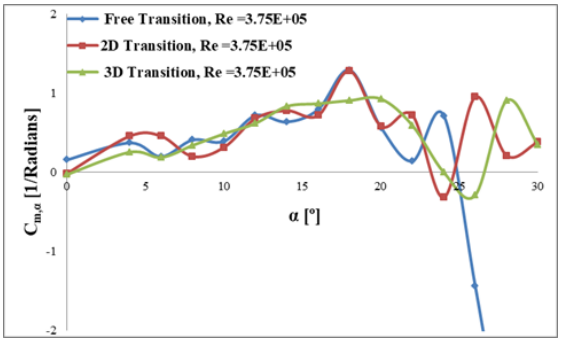

(b)

Figure 11: Pitching moment: (a) Pitching moment, C_m vs. α, (b) Pitching moment derivative C_(m,α) vs. α .

The observed pitching moment characteristics are due to the leading edge vortex flow separation onset and progression over the free transition MULDICON wing, which can be visualised in Figure 8 (a-d). For the higher pitch angle, α≥16º, the $C_{m,\alpha}$ value becomes even more positive. Therefore, not only leading-edge vortex flow separation onset and progression upstream but also the vortex breakdown progression upstream influences the C_m characteristics. Similarly, Figure 11 (b) shows that for the 2D transition derivative $C_{m,\alpha}$ is also unable to maintain the increasing trend, whereas for the 3D transition derivative $C_{m,\alpha}$ is more consistent and follows the increasing trend with the increase in pitch angle, α. For the 3D transition case the trend of the increase in $C_{m,\alpha}$ with the pitch angle,α is disturbed slightly only between α=5-7º for which a slight decrease in $C_{m,\alpha}$ is noticed. Which indicate the onset of the leading-edge vortex. Hence the $C_{m,\alpha}$ the curve for the 3D transition case is more consistent and predictable. Therefore with the application of the 3D transition at the leading edge of the MULDICON wing, the pitching moment coefficient C_m becomes more consistent and predictable up till pitch angle, α 22º by reducing the inconsistencies and the fluctuations of the pitching moment coefficient C_m curve.

The error bar data representing the standard deviation of the time-averaged lift coefficient C_L data logged for different types of transition strips at a speed of 25 m/s is shown in Figure 12 (a). The error bars represent the amount of unsteadiness and uncertainty of the flow topology for different transition strips. Figure 12 (a) shows that the error bars' variance is increasing steadily and gradually with the increase of the pitch angle, α, for all the transition strips cases, and the error bar variance is not significant for any transition strip case. Hence, the unsteadiness and uncertainty of the flow

topology associated with the lift coefficient are not significant. A more detailed analysis of the standard deviation and variance, i.e., the unsteadiness and uncertainty of the flow topology associated with the lift coefficient, can be carried out by plotting the relative standard deviation (RSD) against the pitch angle, α. RSD is used instead of standard deviation to better analyse variance for comparing different data sets. The relative standard deviation RSD is mostly expressed as a percentage, and it is the ratio of the standard deviation, σ to the mean values, ẋ as shown in Eq. (12). Figure 12 (b) shows the graphs for the relative standard deviation RSD of the lift coefficient C_L against the pitch angle, α for different transition strips at speed of 25 m/s, For the free transition cases, the RSD values are higher compared to the 2D and 3D transition for the complete range of pitch angle, whereas overall unsteadiness and uncertainty of the flow topology associated with the lift coefficient are not significant.

$$RSD = \frac{\sigma}{\dot{x}} 100 \tag{12}$$

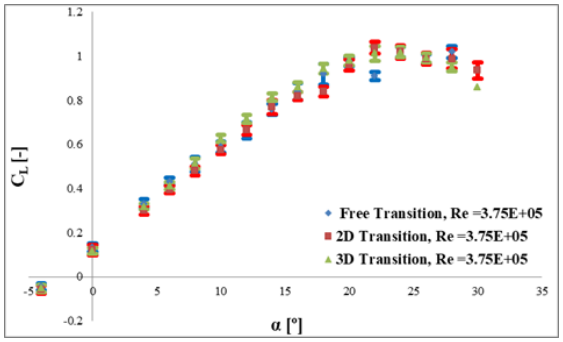

(a)

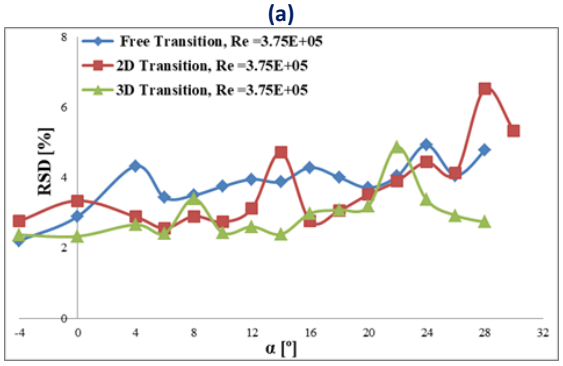

(b)

Figure 12: Standard Deviation data: (a) Error bars Data, C_L vs. α, (b) Relative Standard Deviation for lift vs. α.

The error bar data representing the standard deviation variance of the time-averaged drag coefficient C_D data logged for different types of transition strips at speed of 25 m/s is shown in Figure 13 (a). Figure 13 (a) shows that the error bars variance is increasing with the increase of the pitch angle, α for all the transition strips cases and the error bar variance is more significant for the free transition case at a pitch angle of 4 to 8º and similarly, the error bar variance increased significantly at the higher pitch angles for all the transition strip cases. The errors bars data indicate that the unsteadiness and the uncertainties of the flow topology are more centred on the drag coefficient data. Figure 13 (b) shows the graphs for the relative standard deviation RSD of the drag coefficient C_D against the pitch angle, α for different transition strips at speed of 25 m/s, where it can be seen that the RSD is around 5% at the 0º pitch angle and then increases with the increase in the pitch angle and reaches up to 25% at the higher pitch angles, the RSD for the free transition strip is higher than that for the 2D and 3D transition. Similarly for the free transition cases, the increase in the RSD values is inconsistent and fluctuating with the pitch angle increase and RSD values are higher for the free transition case compared to the 2D and 3D transition cases especially at the smaller pitch angles i.e. α=4 to 14º. The free transition case for the drag analysis is more unsteady and uncertain while the 2D and 3D transition cases predict more consistent and predictable drag coefficient data. Hence the above analysis indicates that the unsteadiness and the uncertainties of the flow topology are more centred on the drag coefficient data compared to the lift coefficient.

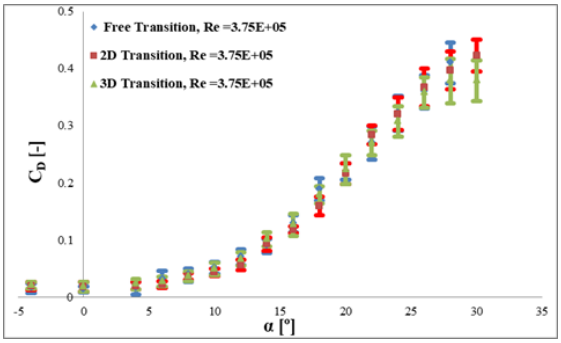

(a)

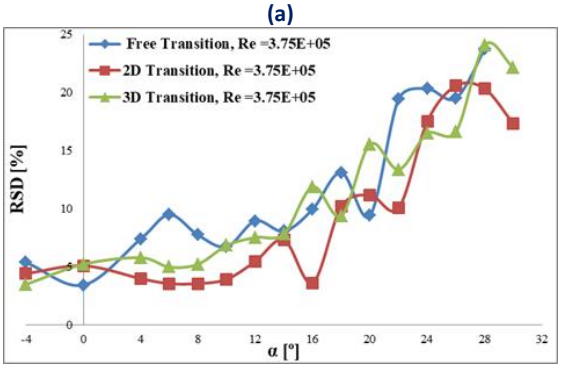

(b)

Figure 13: Standard deviation analysis for drag coefficient: (a) C_D with error bars and (b) relative standard deviation of C_D against pitch angle.

The error bar data representing the standard deviation of the time-averaged pitching moment coefficient C_m data logged for different types of transition strips at a speed of 25 m/s is shown in Figure 14 (a). Figure 14 (a) shows large error bars for the C_m data and the error bars variance is increasing with the increase of the pitch angle,α for 2D and 3D transition strips cases, Figure 14 (a) shows that the error bar variance is more significant for the free transition case at a pitch angle of 4 to 8º probably where the leading edge vortices are formed as shown in Figure 8 (a-d) and similarly the error bar variance increased significantly at the higher pitch angles. The error-bar data for the pitching moment coefficient indicate that unsteadiness and uncertainties in the flow topology significantly affect it.

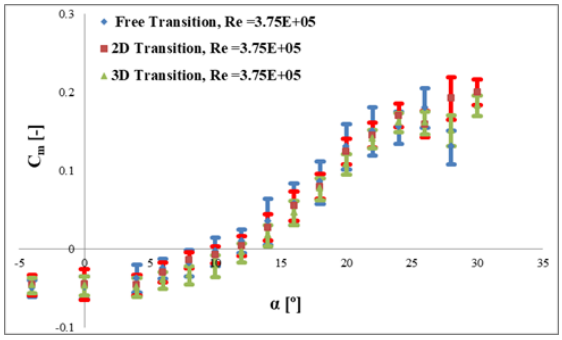

(a)

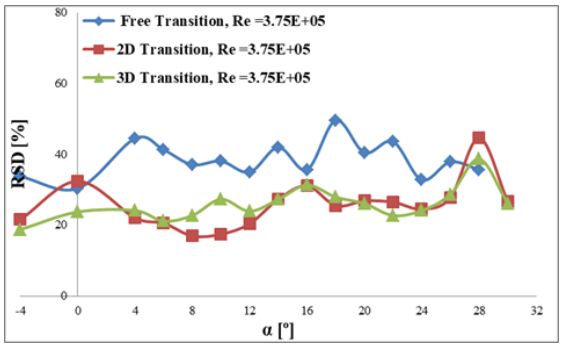

(b)

Figure 14: Standard deviation analysis for pitching-moment coefficient: (a) C_m with error bars and (b) relative standard deviation of C_m against pitch angle.

Figure 14 (b) shows the graphs for the relative standard deviation RSD of the pitching moment coefficient C_m against the pitch angle,α for different transition strips at speed of 25 m/s, where for the 2D and 3D transition strip cases it can be seen that the RSD is varying between 20 to 30% for the complete range of the pitch angle while the variation of the RSD for the 3D transition case is small as compared to the 2D transition case, whereas for the free transition case the RSD is highly inconsistent and fluctuating up to 60% for all range of pitch angle, which reflects highly uncertainty and unsteadiness associated with the free transition case. The statistical analysis of the pitching moment coefficient indicates that unsteadiness and uncertainties in the flow topology significantly affect it; the coefficient is highly sensitive to the flow topology. By applying the 3D transition strips, the inconsistencies and the fluctuations of the pitching moment coefficient are reduced, and the standard deviation is more consistent and predictable.

Influence of Reynolds Number on Aerodynamic Coefficients

The influence of different Reynolds numbers, Re of 3.00E+05, 3.75E+05 and 4.50E+05 corresponding to wind speed of 20, 25, 30 m/s respectively on free transition and 3D transition MULDICON wing are discussed and analysed in this section while running the UTM-LST, for the pitch angle α = -4° to 30° with each increment of 2 degrees.

Aerodynamic Coefficients

An increase in the Re lead to a decrease in the viscous forces and the smooth wall separation is usually dependent on the Reynolds number [1]. In the present example, wall separation is mitigated by the boundary layer's augmented kinetic energy. The Re varies over a small range of 3.00E+05 to 4.50E+05 in the present analysis.

Figure 15 generally shows that the lift coefficient shows no substantial dependence on the Reynold number. Figure 15 (a) for the free transition wing shows that the C_L increase is almost linear before stall with a minor slope decrease, and in this range of pitch angle, the Re variation does not influence the lift coefficient. However, some deviations are detected about the higher pitch angles i.e. α > 22º. The flow topology at very high pitch angles is vortex-collapse-dominated rather than vortex-dominated, which is more sensitive to . Therefore, a slight higher OBJ value is obtained at 3.00E+05 due to the further upstream leading-edge separation, while OBJ at both the highest freestream Reynolds numbers are similar. Figure 15 (b) shows that the Reynold number dependence behaviour differs slightly for the 3D transition case with the slight variations with the $C_{L,max}$ values for the lowest analysed Re have increased accordingly.

Figure 16 (a) for the free transition wing case shows that there is no major influence of the Reynolds number on the drag coefficient with

slight variations at higher pitch angles, whereas for the 3D transition case Figure 16 (b) shows that the drag coefficient is more Reynolds number dependent and especially at higher pitch angles there appears the significant influence of the Reynolds number on the drag coefficient.

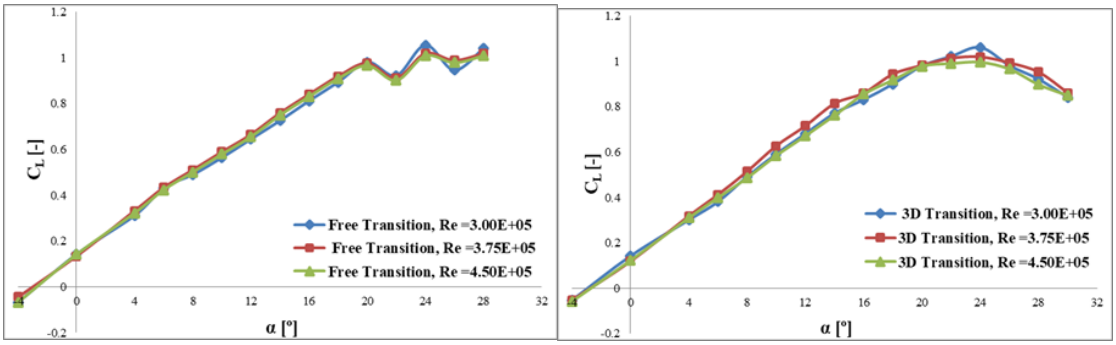

(a) (b)

Figure 15: Lift Coefficient: (a) Free Transition, C_L against α, (b) 3D Transition C_L against α.

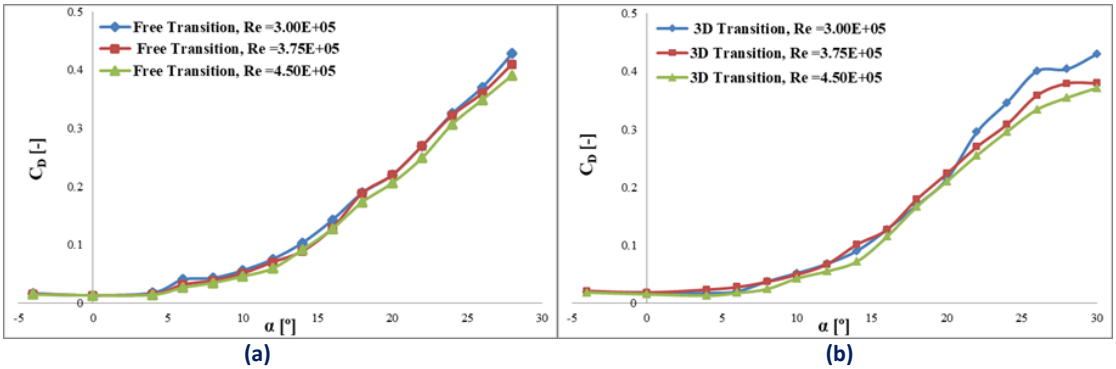

(a) (b)

Figure 16: Drag Coefficient: (a) Free Transition, C_D against α, (b) 3D Transition C_D against α.

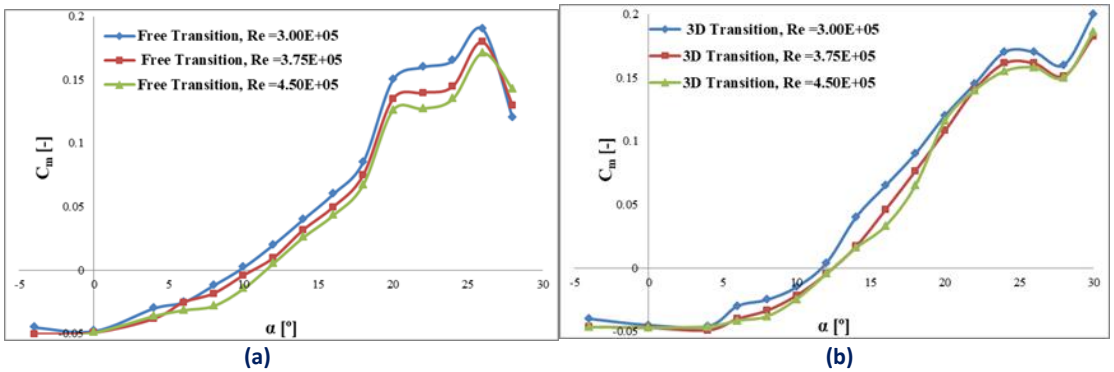

(a) (b)

Figure 17: Pitching moment coefficient: (a) Free Transition, C_m against α, (b) 3D Transition C_L against α.

Figure 17 (a) for the free transition wing indicates that the increasing Re has the effect of delaying pitch-up to a slightly higher pitch angle only. The influence of the Re on the pitching moment coefficient is observed at much lower pitch angles than that for the lift and drag curves, as low as α=5º. The Re influence is somewhat greater at higher Re i.e. 4.50E+05 at or near the pitch up angles. For higher pitch angles the Re influence is rather small. Similarly, Figure 17 (b) for the 3D transition wing also indicates that increasing Re has the effect of delaying pitch-up to a slightly higher pitch angle. C_m increase with a decrease in Reynolds number for a wide range of pitch angles

of α=4 to 22º, the region where the leading-edge vortex is developed over the major part of the MULDICON wing. Similarly, for higher pitch angles the Re influence is rather small for the 3D transition case also. Therefore, the Reynolds number dependent pitching moment coefficient is caused by Reynolds number dependent vortex separation onset and progression location.

Uncertainty analysis

The error bar data and the RSD in Figure 18 (a) & (c), for the free transition case shows that the lift coefficient C_L shows no substantial dependency on the Reynold number for the almost complete range of pitch angle. Whereas Figure 18 (b) & (d) shows that for the 3D transition case there is a certain influence of the Reynold number on the lift coefficient, C_L especially at higher pitch angles, α.

The error bar data and the RSD in Figure 19 (a) & (c), shows that for the free transition case the drag coefficient, C_D shows no dependency on the Reynold number for the lower pitch angle range but at high pitch angles, some variation with the Reynolds number is observed. Whereas Figure 19 (b) & (d) shows that for the 3D transition case the error bars are bigger with the Reynolds number variation and the RSD is more inconsistent and fluctuating. Hence Figure 19 indicates that there is a definite influence of the Reynolds number for the 3D transition wing configuration. The error bar data and the RSD in Figure 20 (a) & (c), shows that for the free transition case the pitching moment coefficient, C_m shows no dependency on the Reynold number for the lower pitch angle range but at high pitch angles, some variation with the Reynold number is observed. Whereas Figure 20 (b) & (d) for the 3D transition case shows that there is a significant influence of the Reynolds number for the complete range of the pitch angle. Hence, the error bar data and the RSD data confirm that for the free transition wing, there is no or very little influence of the Reynold number on the aerodynamic coefficients, whereas for the 3D transition case, there is a significant influence of the Reynold number on the aerodynamic coefficients.

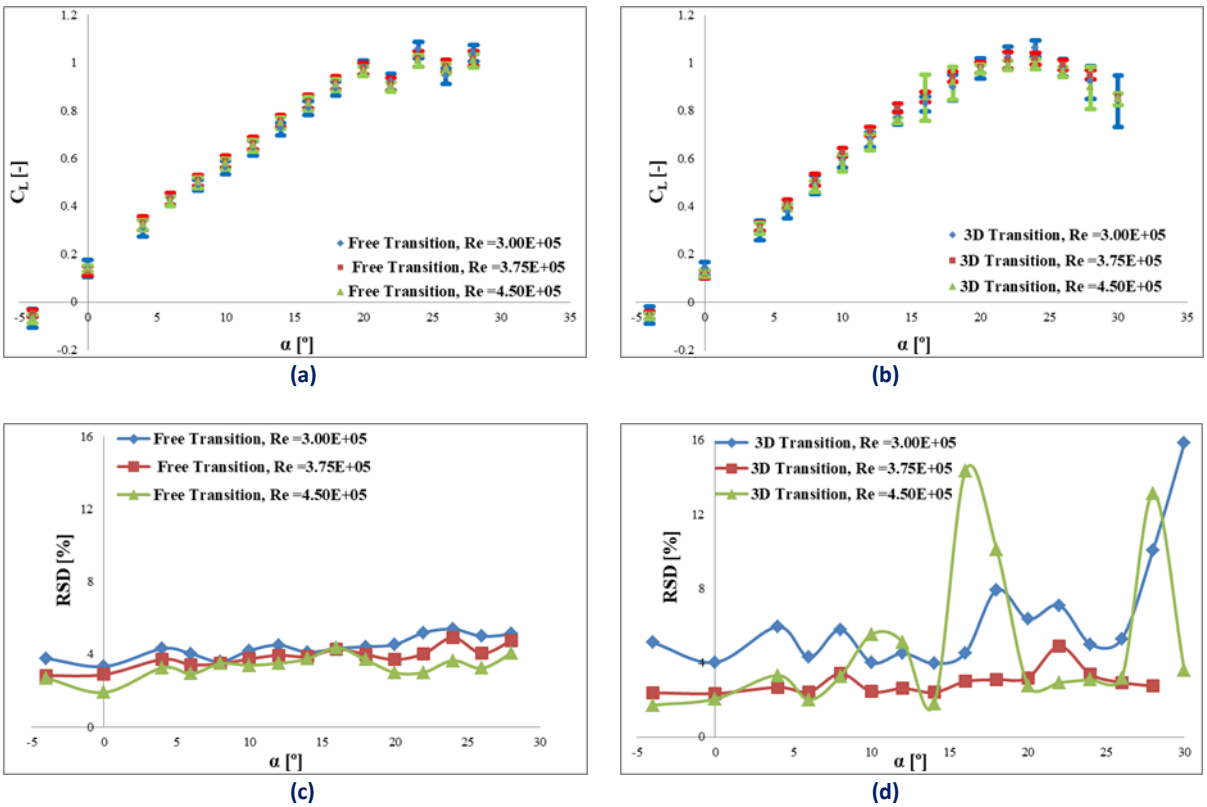

Figure 18: Standard Deviation data: (a) Error bars Data, C_L against α (Free transition), (b) Error bars Data, C_L against α (3D transition), (c) RSD for a lift against α (Free transition), (d) RSD for lift against α (3D transition).

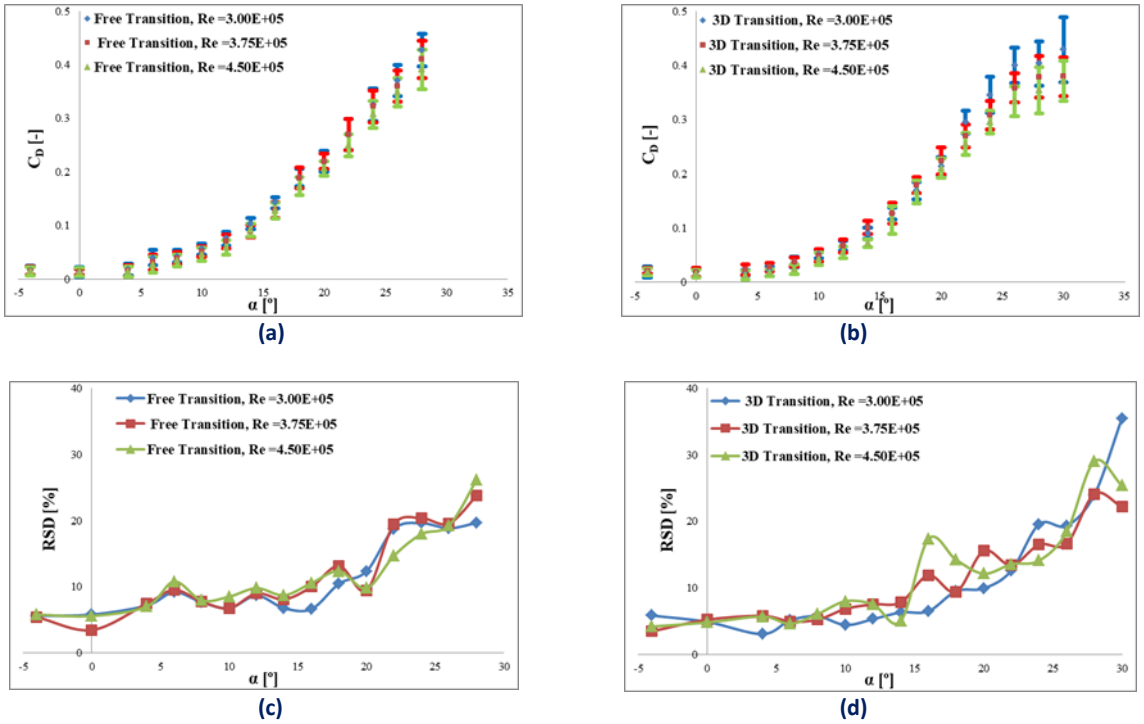

Figure 19: Standard Deviation data: (a) Error bars Data, C_D against α (Free transition), (b) Error bars Data, C_D against α (3D transition), (c) RSD for C_D against α (Free transition), (d) RSD for C_D against α (3D transition).

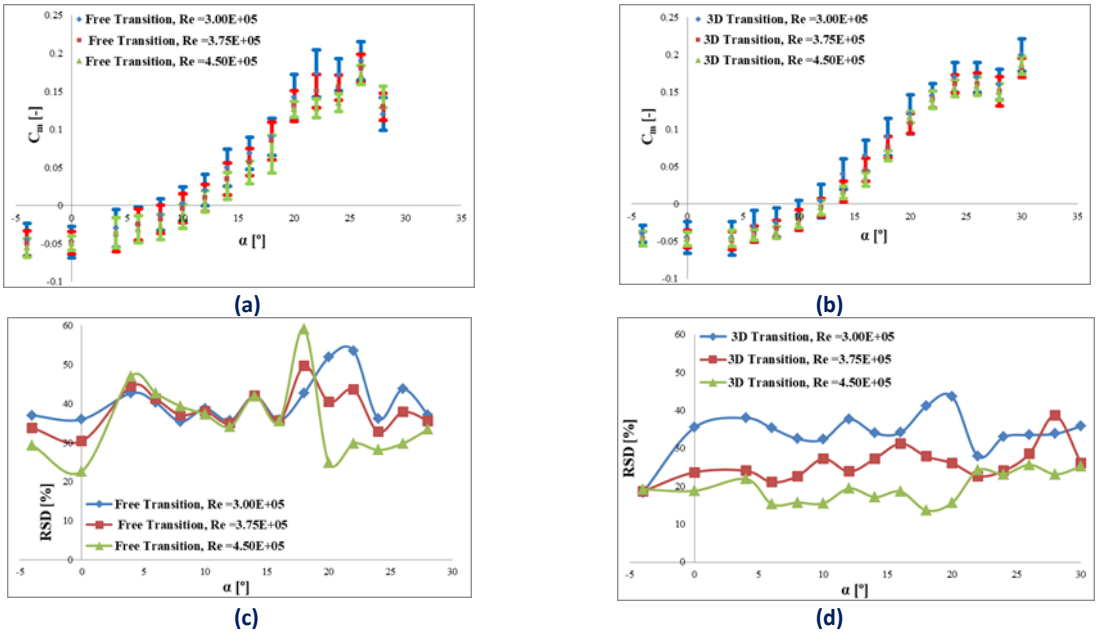

Figure 20: Standard Deviation data: (a) Error bars Data, C_m vs. α (Free transition), (b) Error bars Data, C_m vs. α (3D transition), (c) RSD for C_m vs. α (Free transition), (d) RSD for C_m vs. α (3D transition).

Discussion

Based on the results presented, a strong correlation between flow topology and pitching moment coefficient is exhibited in experimental investigations of the MULDICON wing, as predicted previously by Vandam [44], McParlin, Bruce [45], Schütte, Hummel [46], Coppin, Birch [47]. For Reynolds number Re= 4.50E+05, Figure 21 shows that at low pitch angles, until α ≈ 6° the pitching moment changes linearly with pitch angle, which suggests that there will be completely attached

flow with no leading-edge vortex formed over the MULDICON wing surface for pitch angle, α<6º and can be seen with the flow visualisation at α=5º as in Figure 8 (a). When α ≥ 6°, the increase in the pitching moment is no longer linear, as shown in Figure 21. The pitching moment increases in a nonlinear manner, which suggests that at this pitch angle, the LE vortex flow separation onset and progression start. The onset of the LE vortex flow separation near the wingtip is visualised at α=10° in Figure 8 (b). The LE vortex appears and moves upstream as the pitch angle α increases, as shown in Figure 8 (a-d).

With the further increase in the pitch angle, α when the tip vortex and the vortex breakdown moves further upstream towards the apex of the wing and defeats the moment reference point (MRP) as shown in Figure 8 (d), a rapid pitch-up moment is generated as previously predicted by Coppin, Birch [47] which can be correlated in Figure 21 for pitch angles, α≥17º, where the pitching moment curve becomes steeper which indicates the extra pitch up possibly due to the onset and progression of the vortex breakdown within the tip vortex. As the pitch angle increases, the leading-edge vortex and associated breakdown region move upstream towards the moment reference point. This changes the pressure distribution over the upper surface and shifts the resultant aerodynamic load relative to the moment reference centre. The altered load distribution can increase the nose-up pitching moment, producing the observed pitch-up trend at higher pitch angles.

The free-transition case at Re=4.50×10^5 was selected for Figure 21 because the corresponding surface oil-flow visualisation was available for this condition, allowing direct comparison between observed vortex topology and pitching-moment behaviour. The 2D and 3D transition cases are not included in this correlation because equivalent surface-flow visualisation images were not obtained under identical conditions. However, their aerodynamic coefficient trends are discussed separately to evaluate the influence of transition-strip type.

Therefore, a strong correlation is present between the Pitching moment derivative and the flow visualisation, which is validated by comparing the pitching moment with the flow topology in Figure 8 (a-d) and Figure 21. The standard deviation data for the pitching moment coefficient also indicate that unsteadiness and uncertainties in the flow topology significantly affect it. Hence, the pitching moment coefficient is very sensitive to the flow topology.

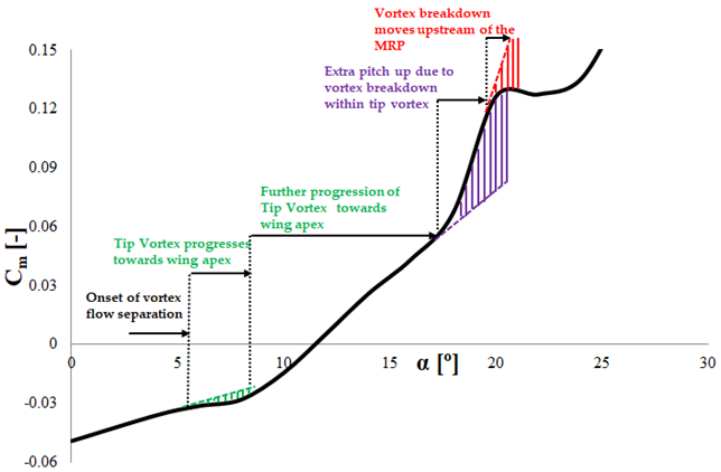

Figure 21: Possible influence of the vortex flow topology on the pitching moment analysis, free transition MULDICON wing at Re= 4.50E+05.

Surface flow visualisation at higher pitch angles (α > 20º) needs to be carried out to examine the flow topology. The influence of lift, drag, and pitching moment should be further studied over a wide range of Reynolds numbers. Some Particle Image Velocimetry (PIV) or hotwire anemometry method should be carried out in future to quantify the strength of the LE vortex, the inner vortex, the apex vortex and the vortex breakdown above the surface of the MULDICON wing. Yaw moment $C_{n,\beta}$ and Side force moment $C_{y,\beta}$ should also be studied in future work at various pitch angles, α so that some correlation between the aerodynamic stability derivatives could be developed. Dynamic stability derivatives should also be investigated in future.

CONCLUSION

This study investigated the influence of leading-edge transition strips on the aerodynamic behaviour of a low-sweep, blunt-leading-edge MULDICON AVT251 wing using low-speed wind-tunnel testing. Free-transition, 2D-transition, and 3D-transition cases were compared using force and moment measurements, surface oil-flow visualisation, and uncertainty analysis. The influence of different transition strips shows that the 3D transition case predicts a rather smooth and consistent lift curve and the stall is predicted at α = 24° where the C_L = 1.0183, whereas the free transition and 2D transition cases fail to predict stall angle as the lift curve is fluctuating at higher pitch angles. The 3D transition case gives lower C_D at higher pitch angles, with an increase of $C_{D,0}$ noticed. The 3D transition case predicts a more consistent and predictable pitching moment coefficient C_m curve up to pitch angle,α of 22° compared to the free and 2D transition cases, by reducing the inconsistencies and the fluctuations of the pitching moment curve.

The relative standard deviation (RSD) for the lift coefficient is between 4% and 6% across all transition cases, indicating that the overall unsteadiness and uncertainty in the flow topology associated with the lift coefficient are not significant. The RSD for the drag coefficient is between 5-25% across all transition cases, indicating that the unsteadiness and uncertainties in the flow topology are more pronounced in the drag coefficient data than in the lift coefficient, with the free transition case drag appearing most unsteady. The RSD for the pitching moment coefficient is between 18-55% for all transition cases which indicate that the unsteadiness and the uncertainties of the flow topology significantly affect the pitching moment coefficient, therefore the pitching moment coefficient is very sensitive to the flow topology, while for the 3D transition strips the unsteadiness and uncertainties of the pitching moment coefficient are reduced with RSD less than 22-30% for all range of pitch angle.

The lift coefficient C_L shows no substantial dependence on the Reynolds number in both free and 3D transition cases. The drag coefficient C_D shows no dependency on the Re for the free transition case, whereas the 3D transition wing appears to be Re dependent. The Reynolds number influences the pitching-moment coefficient C_m for both the free-transition and 3D-transition cases in the nonlinear region where the leading-edge vortex develops. Therefore, the Reynolds number-dependent pitching moment coefficient is caused by Reynolds number-dependent vortex separation onset and progression location. In the standard deviation data for the free transition wing, there is no or very little influence of the Reynold number on the aerodynamic coefficients, whereas for the 3D transition case, there is a significant influence of the Reynold number on the aerodynamic coefficients. A strong correlation between flow topology and the pitching moment coefficient is observed, indicating that uncertainties in unsteadiness and flow topology significantly affect the coefficient and render it highly sensitive to these variables.

ACKNOWLEDGEMENT

This research was funded by the Universiti Teknologi Malaysia (Grant 21H05). Special acknowledgement to the technical staff of the Universiti Teknologi Malaysia Aerolab. The main author acknowledges the Higher Education Commission for funding PhD study.

REFERENCES

[1] *Anderson, D., Graham, I., & Williams, B. (2015). Flight and motion (pp. 14–19). Routledge.*
[2] *Polhamus, E. C. (1966). A concept of the vortex lift of sharp-edge delta wings based on a leading-edge-suction analogy.*
[3] *Gursul, I. (2004). Recent developments in delta wing aerodynamics. The Aeronautical Journal, 108(1087), 437–452.*
[4] *Rockwell, D. (1993). Three-dimensional flow structure on delta wings at high angle-of-attack—Experimental concepts and issues. In 31st Aerospace Sciences Meeting.*
[5] *Visbal, M. (1995). Computational and physical aspects of vortex breakdown on delta wings. In 33rd Aerospace Sciences Meeting and Exhibit.*
[6] *Gursul, I., Gordnier, R., & Visbal, M. (2005). Unsteady aerodynamics of nonslender delta wings. Progress in Aerospace Sciences, 41(7), 515–557.*
[7] *Ghoreyshi, M., et al. (2016). Vortical flow prediction of a diamond wing with rounded leading edges. Aerospace Science and Technology, 57, 103–117.*
[8] *Hövelmann, A., & Breitsamter, C. (2015). Leading-edge geometry effects on the vortex formation of a diamond-wing configuration. Journal of Aircraft, 52(5), 1596–1610.*
[9] *Osterhuber, R. (2013). FCS requirements for future LO combat aircraft. STO/AVT-215 Workshop on Innovative Control Effectors for Military Vehicles.*

[10] Yaniktepe, B., & Rockwell, D. (2004). Flow structure on a delta wing of low sweep angle. AIAA Journal, 42(3), 513–523.
[11] Ol, M. V., & Gharib, M. (2003). Leading-edge vortex structure of nonslender delta wings at low Reynolds number. AIAA Journal, 41(1), 16–26.
[12] Renac, F., Barberis, D., & Molton, P. (2005). Control of vortical flow over a rounded leading-edge delta wing. AIAA Journal, 43(7), 1409–1418.
[13] Gordnier, R., & Visbal, M. (2003). Higher-order compact difference scheme applied to low sweep delta wing flow. In 41st Aerospace Sciences Meeting and Exhibit.
[14] Paul, M., & Rein, M. (2016). Transonic numerical and experimental investigation into unconventional lambda wing control surfaces. In 54th AIAA Aerospace Sciences Meeting.
[15] Hummel, D. (2004). Effects of boundary layer formation on the vortical flow above slender delta wings. In Enhancement of NATO Military Flight Vehicle Performance by Management of Interacting Boundary Layer Transition and Separation.
[16] Huri, Shabudin, & Mazuriah. (2018). Experimental investigation on blunt-edged UTM delta wing VFE-2 configurations at low Reynolds number. International Review of Mechanical Engineering (IREME), 12(3).
[17] Loeser, T., Vicroy, D., & Schuette, A. (2010). SACCON static wind tunnel tests at DNW-NWB and 14 × 22 NASA LaRC. In 28th AIAA Applied Aerodynamics Conference.
[18] Nangia, R., Boelens, O., & Tormalm, M. (2010). A tale of two UCAV wing designs. In 28th AIAA Applied Aerodynamics Conference.
[19] Schuette, A., et al. (2018). Aerodynamic shaping design and vortical flow design aspects of a 53° swept flying wing configuration. In 2018 Applied Aerodynamics Conference.
[20] Cummings, R. M., & Schütte, A. (2012). Integrated computational/experimental approach to unmanned combat air vehicle stability and control estimation. Journal of Aircraft, 49(6), 1542–1557.
[21] Cummings, R., Schütte, A., & Hübner, A. (2013). Overview of stability and control estimation methods from NATO STO Task Group AVT-201. In 51st AIAA Aerospace Sciences Meeting Including the New Horizons Forum and Aerospace Exposition.
[22] Hitzel, S. M., et al. (2016). Vortex development on the AVT-183 diamond wing configuration—Numerical and experimental findings. Aerospace Science and Technology, 57, 90–102.
[23] Hövelmann, A., Knoth, F., & Breitsamter, C. (2016). AVT-183 diamond wing flow field characteristics Part 1: Varying leading-edge roughness and the effects on flow separation onset. Aerospace Science and Technology, 57, 18–30.
[24] Hövelmann, A., et al. (2016). AVT-183 diamond wing flow field characteristics Part 2: Experimental analysis of leading-edge vortex formation and progression. Aerospace Science and Technology, 57, 31–42.
[25] Aref, P., et al. (2017). Preliminary computational aerodynamic investigation of the NATO AVT 251 multi-disciplinary configuration. In 35th AIAA Applied Aerodynamics Conference.
[26] Kaya, H., et al. (2018). A multi-fidelity aerodynamic modelling approach for NATO AVT 251 UCAV–MULDICON. In 2018 Applied Aerodynamics Conference.
[27] Nangia, R., et al. (2019). Aerodynamic design assessment and comparisons of the MULDICON UCAV concept. Aerospace Science and Technology, 93, 105321.
[28] van Rooij, M., & Cummings, R. M. (2018). Aerodynamic design of an unmanned combat air vehicle in a collaborative framework. In 2018 Applied Aerodynamics Conference.
[29] Noor, A., & Mansor, S. (2013). Measuring aerodynamic characteristics using high performance low speed wind tunnel at Universiti Teknologi Malaysia. Journal of Applied Mechanical Engineering, 3(132), 1–7.
[30] Elfstrom, G. (2007). History of test facility design expertise at Aiolos Engineering Corporation. In 45th AIAA Aerospace Sciences Meeting and Exhibit.
[31] White, F. M., & Corfield, I. (2006). Viscous fluid flow (Vol. 3). McGraw-Hill.
[32] Barlow, J. B., Rae, W. H., Jr., & Pope, A. (2015). Low-speed wind tunnel testing. INCAS Bulletin, 7(1), 133.
[33] Laster, M. (1988). Boundary layer simulation and control in wind tunnels (AGARD Advisory Report No. 224).
[34] Gersten, K. (2009). Hermann Schlichting and the boundary-layer theory. In Hermann Schlichting–100 Years (pp. 3–17). Springer.
[35] Giguère, P., & Selig, M. S. (1999). Aerodynamic effects of leading-edge tape on aerofoils at low Reynolds numbers. Wind Energy, 2(3), 125–136.
[36] Vicroy, D. D., et al. (2014). Low-speed dynamic wind tunnel test analysis of a generic 53° swept UCAV configuration. In 32nd AIAA Applied Aerodynamics Conference.
[37] Buzica, A., et al. (2018). Leading-edge roughness affecting diamond-wing aerodynamic characteristics. Aerospace, 5(3), 98.
[38] Breitsamter, C. (2006). Strömungsphysik und Modellgesetze. Lecture handout, Technische Universität München.
[39] Schlichting, H., & Gersten, K. (2006). Grenzschicht-Theorie. Springer-Verlag.
[40] Houghton, E., Carpenter, P., Collicott, S. H., & Valentine, D. T. (2013). Aerodynamics for engineering students.
[41] Anderson, J. D., Jr. (n.d.). Introduction to flight.
[42] Taylor, G. S., & Gursul, I. (2004). Buffeting flows over a low-sweep delta wing. AIAA Journal, 42(9), 1737–1745.
[43] Loechert, P., et al. (2018). Control device studies for yaw control without vertical tail plane on a 53° swept flying wing configuration. In 2018 Applied Aerodynamics Conference.

[44] Vandam, C. P. (1989). High angle-of-attack aerodynamic characteristics of crescent and elliptic wings.

[45] McParlin, S., et al. (2006). Low speed wind tunnel tests on the 1303 UCAV concept. In 24th AIAA Applied Aerodynamics Conference.

[46] Schütte, A., Hummel, D., & Hitzel, S. M. (2010). Numerical and experimental analyses of the vortical flow around the SACCON configuration. In 28th AIAA Applied Aerodynamics Conference.

[47] Coppin, J., et al. (2016). Prediction of control effectiveness for a highly swept unmanned air vehicle configuration. Journal of Aircraft, 55(2), 534–548.